

# Enhanced charge transport and increased active sites on $\alpha$ -Fe<sub>2</sub>O<sub>3</sub> (110) nanorod surface containing oxygen vacancies for improved solar water oxidation performance

Hu, Jun; Zhao, Xin; Chen, Wei; Chen, Zhong

2018

Hu, J., Zhao, X., Chen, W., & Chen, Z. (2018). Enhanced charge transport and increased active sites on  $\alpha$ -Fe<sub>2</sub>O<sub>3</sub> (110) nanorod surface containing oxygen vacancies for improved solar water oxidation performance. ACS Omega, 3(11), 14973-14980.  
doi:10.1021/acsomega.8b01195

<https://hdl.handle.net/10356/105571>

<https://doi.org/10.1021/acsomega.8b01195>

---

© 2018 American Chemical Society. All rights reserved. This paper was published in ACS Omega and is made available with the permission of American Chemical Society.

*Downloaded on 27 Aug 2022 23:55:48 SGT*



# Enhanced Charge Transport and Increased Active Sites on $\alpha$ -Fe<sub>2</sub>O<sub>3</sub> (110) Nanorod Surface Containing Oxygen Vacancies for Improved Solar Water Oxidation Performance

Jun Hu,<sup>†,‡,||</sup> Xin Zhao,<sup>\*,‡,||</sup> Wei Chen,<sup>‡,§</sup> and Zhong Chen<sup>\*,‡,||</sup>

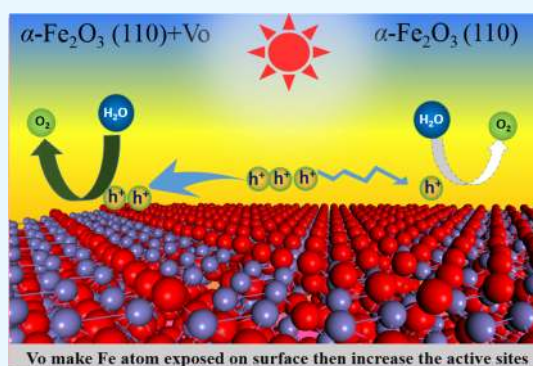
<sup>†</sup>School of Chemical Engineering, Northwest University, Xi'an 710069, P. R. China

<sup>‡</sup>School of Materials Science and Engineering, Nanyang Technological University, 50 Nanyang Avenue, 639798, Singapore

<sup>§</sup>School of Pharmaceutical and Chemical Engineering, Taizhou University, Taizhou 318000, Zhejiang Province, P. R. China

## Supporting Information

**ABSTRACT:** The effect of oxygen vacancies ( $V_O$ ) on  $\alpha$ -Fe<sub>2</sub>O<sub>3</sub> (110) facet on the performance of photoelectrochemical (PEC) water splitting is researched by both experiments and density functional theory (DFT) calculations. The experimental results manifest that the enhancement in photocurrent density by the presence of  $V_O$  is related with increased charge separation and charge-transfer efficiencies. The electrochemical analysis reveals that the sample with  $V_O$  demonstrates an enhanced carrier density and reduced charge-transfer resistance. The results of DFT calculation indicate that the better charge separation is also contributed by the decrease of potential on the  $V_O$  surface, which improves the hole transport from the bulk to the surface. The reduced charge-transfer resistance is owing to the greatly increased number of active sites. The current study provides important insight into the roles of  $V_O$  on  $\alpha$ -Fe<sub>2</sub>O<sub>3</sub> photoanode, especially on its surface catalysis. The generated lesson is also helpful for the improvement of other PEC photoanode materials.



## 1. INTRODUCTION

A photoelectrochemical (PEC) water-splitting cell can convert electromagnetic energy into storable chemical energy without causing pollution in the process. Among the photoanode materials for PEC, hematite ( $\alpha$ -Fe<sub>2</sub>O<sub>3</sub>) has received much attention as an efficient, robust, and inexpensive photoelectrode material for on-demand oxygen production.<sup>1</sup> Since Hardee et al. first used Fe<sub>2</sub>O<sub>3</sub> for water splitting in 1976, considerable effort has been devoted to improve its activity through doping,<sup>2–6</sup> heterojunction formation,<sup>7,8</sup> morphology control,<sup>9–12</sup> and so forth. However, there is still a long way to go because of its poor conductivity, low flat band potential, short diffusion length, and large overpotential for water oxidation.<sup>13</sup>

The past researches on photocatalytic materials have found that manipulating crystalline defects is as important as the morphology control. Defects engineering has thus become an attractive avenue for improving the energy-harvesting performance along with other conventional approaches. Oxygen vacancy ( $V_O$ ) is one of the most important defects in metal oxides. Recent experimental results indicate that  $V_O$  on the surface can enhance electron transport.<sup>14–24</sup> It has been found that  $V_O$  can improve the PEC efficiency by increasing the density and mobility of holes for improved electron–hole separation.<sup>25</sup> For Fe<sub>2</sub>O<sub>3</sub>, Ling et al. found the performance of pristine hematite nanorod to be greatly enhanced because of

the formation of  $V_O$  by thermal treatment in an oxygen-deficient atmosphere.<sup>26</sup> Dieckmann pointed out that  $V_O$  is the dominant ionic defect in hematite on the basis of electrical conductance data.<sup>27</sup> Chen et al. observed two types of  $V_O$  in Fe<sub>2</sub>O<sub>3</sub> nanowires and nanobelts ( $\bar{3}30$ ) and (112) facets.<sup>28</sup> Apart from the experimental work, the effect of  $V_O$  on the electronic structure was also researched theoretically. Warschkow et al. found that it is thermodynamically possible for a higher concentration of  $V_O$  to exist on the surface than in the bulk.<sup>29</sup> It was also found that the presence of Au particles, especially semi-oxidized Au, can remarkably reduce the formation energy of  $V_O$  on the  $\alpha$ -Fe<sub>2</sub>O<sub>3</sub>(001) surface.<sup>30</sup> Song et al. indicated that  $V_O$  on the  $\alpha$ -Fe<sub>2</sub>O<sub>3</sub>(001) surface greatly strengthens the adsorption of NO and H<sub>2</sub>O<sub>2</sub>, which can largely improve the ability of H<sub>2</sub>O<sub>2</sub> decomposition.<sup>31</sup> Despite the fact that  $V_O$  on Fe<sub>2</sub>O<sub>3</sub> has received considerable attention recently, most of them focused on the electronic property. As known, the oxygen evolution reaction (OER) is an energetically uphill process.<sup>32–34</sup> However, information on  $V_O$  on the  $\alpha$ -Fe<sub>2</sub>O<sub>3</sub> (110) facet that induced charge transport and separation during the water-splitting process is still missing from the literature. Therefore, a detailed knowledge about charge

Received: June 3, 2018

Accepted: October 23, 2018

Published: November 6, 2018

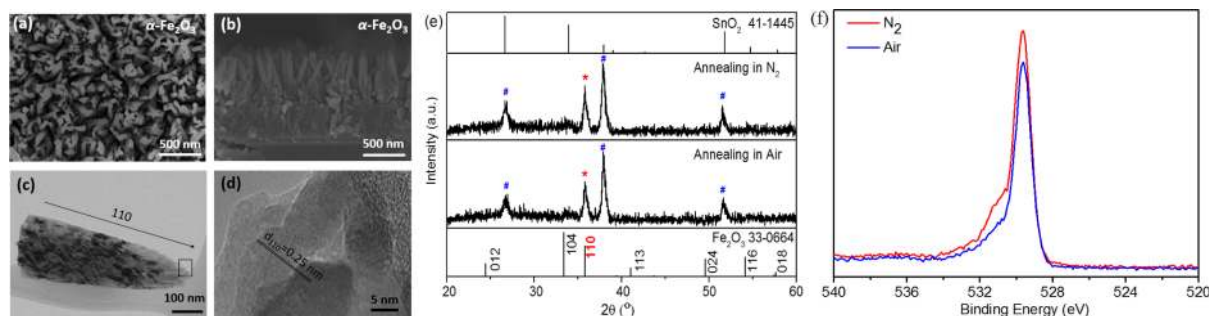


**Figure 1.** Microstructure of  $\alpha$ -Fe<sub>2</sub>O<sub>3</sub>. (a) SEM morphologies; (b) cross-sectional images; (c) TEM images; (d) higher resolution image corresponding to the rectangle area of TEM; (e) XRD after treatment in nitrogen gas and air; and (f) O 1s XPS spectra with different treatments.

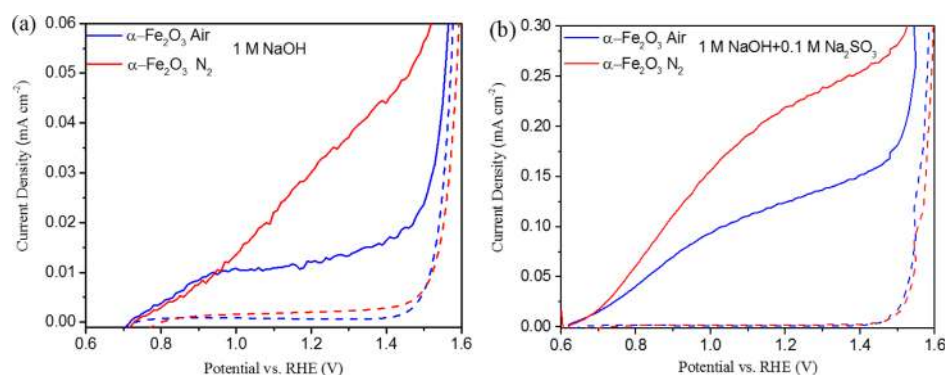


**Figure 2.** Photocurrents of  $\alpha$ -Fe<sub>2</sub>O<sub>3</sub> in (a) 1 M NaOH solution and (b) 1 M NaOH + 0.1 M Na<sub>2</sub>SO<sub>3</sub> with and without nitrogen treatment under an AM 1.5 G solar simulator illumination. Solid lines are photocurrents and dotted lines are dark currents.

distribution on defect-free or V<sub>O</sub>-containing surfaces is necessary for a fundamental understanding of the effect of V<sub>O</sub>.<sup>35</sup> In the present study, a systematic experimental and quantum chemical simulation on the roles of V<sub>O</sub> is presented using  $\alpha$ -Fe<sub>2</sub>O<sub>3</sub> nanorod with exposed (110) facets. The experimental results indicate that V<sub>O</sub> on the  $\alpha$ -Fe<sub>2</sub>O<sub>3</sub> (110) facet has indeed increased the activity of OER. Theoretical analysis found that V<sub>O</sub> can enhance hole transport and increase the transfer efficiency by reducing the potential and increasing the density of the active sites.

## 2. RESULTS AND DISCUSSION

**2.1. Microstructure of Fe<sub>2</sub>O<sub>3</sub> Thin Films.** Nanorod-structured  $\alpha$ -Fe<sub>2</sub>O<sub>3</sub> thin films with a thickness of 500 nm were prepared (Figure 1a,b). The selected area electron diffraction (SAED) patterns and the high-resolution transmission electron microscopy (HRTEM) images suggest that the exposed facet for this nanorod is the (110) plane. X-ray diffraction (XRD) (Figure 1e) shows that this material belongs to hematite (PDF#33-0664). The main peak belongs to the (110) plane, which also confirms the TEM results that the nanorod grows along the [110] direction. No impurity peaks were present except the FTO (SnO<sub>2</sub>) substrate. Moreover, the crystal structure was not changed after the nitrogen treatment. Figure 1f shows the chemical state of O 1s by X-ray photoelectron spectroscopy (XPS). Both samples have the same binding energy at 529.6 eV, assigned to the lattice oxygen. A shoulder peak at 531.0 eV appears for the N<sub>2</sub>-treated sample. This is an evidence for the existence of V<sub>O</sub> on the  $\alpha$ -Fe<sub>2</sub>O<sub>3</sub>(001) surface.<sup>36,37</sup>

**2.2. OER Performance of Fe<sub>2</sub>O<sub>3</sub> Thin Films.** Figure 2a manifests the photocurrents of  $\alpha$ -Fe<sub>2</sub>O<sub>3</sub> with and without a

hole scavenger. Before the nitrogen treatment, the maximum photocurrent density for defect-free  $\alpha$ -Fe<sub>2</sub>O<sub>3</sub> was around 0.016 mA·cm<sup>-2</sup> at 1.23 V<sub>RHE</sub>, whereas the one after nitrogen treatment was around 0.038 mA·cm<sup>-2</sup>, which corresponds to a 137% increase. As shown in Figure 2a,b, the oxidation photocurrents in the Na<sub>2</sub>SO<sub>3</sub> solution are significantly enhanced after the N<sub>2</sub> treatment. This implies that the N<sub>2</sub> treatment mainly alters the bulk charge separation. Further quantitative analysis will be given and discussed next.

As shown in Table 1, the charge separation efficiency of  $\alpha$ -Fe<sub>2</sub>O<sub>3</sub> annealed in air is only about 1.1% at 1.23 V<sub>RHE</sub>, whereas

**Table 1.** Calculated  $\eta_{\text{sep}}$  and  $\eta_{\text{tran}}$  of  $\alpha$ -Fe<sub>2</sub>O<sub>3</sub> before and after N<sub>2</sub> Heat Treatment

sample	treatment	$\eta_{\text{sep}}$ (%)	$\eta_{\text{tran}}$ (%)
$\alpha$ -Fe <sub>2</sub> O <sub>3</sub>	Air	1.1	8.7
$\alpha$ -Fe <sub>2</sub> O <sub>3</sub>	N <sub>2</sub>	2.2	15.2

that of  $\alpha$ -Fe<sub>2</sub>O<sub>3</sub> annealed in N<sub>2</sub> is about 2.2%. The charge-transfer efficiency of  $\alpha$ -Fe<sub>2</sub>O<sub>3</sub> is about 8.7% at 1.23 V<sub>RHE</sub> and that of  $\alpha$ -Fe<sub>2</sub>O<sub>3</sub> annealed in N<sub>2</sub> is about 15.2%. As a result, the improved performance is contributed by both increased hole separation and transfer. The amounts of generated H<sub>2</sub> and O<sub>2</sub> are listed in Figure S1.

Mott–Schottky plots of  $\alpha$ -Fe<sub>2</sub>O<sub>3</sub> after N<sub>2</sub> and air heat treatment were used to estimate the electron density (Figure 3a) by eq 1<sup>38</sup>

$$N_d = (2/e_0\epsilon\epsilon_0A^2)[d(1/C^2)/dV]^{-1} \quad (1)$$

where  $e_0$ ,  $\epsilon$ , and  $\epsilon_0$  are the electron charge with a value of 1.60  $\times 10^{-19}$  C, dielectric constant with a value of 80,<sup>39</sup> and permittivity of vacuum with a value of 8.85  $\times 10^{-12}$  F·m<sup>-1</sup>,

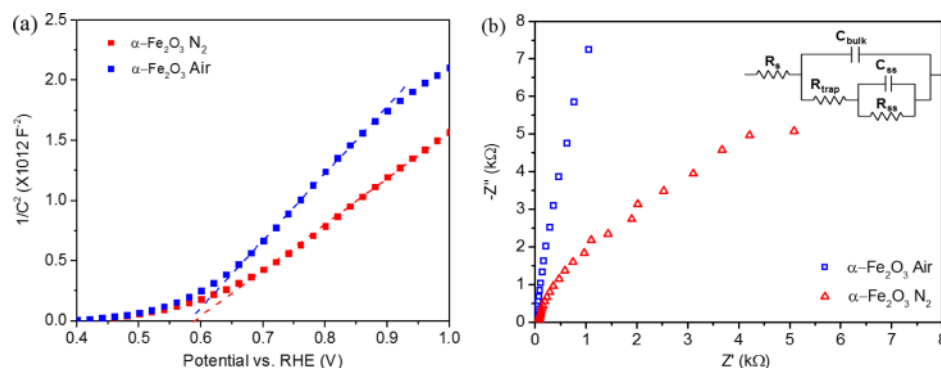


**Figure 3.** (a) Mott–Schottky plots at 1000 Hz of  $\alpha\text{-Fe}_2\text{O}_3$  after N<sub>2</sub> and air heat treatment. (b) Nyquist plots of  $\alpha\text{-Fe}_2\text{O}_3$  with the frequency range from 1 to  $10^5$  Hz before and after N<sub>2</sub> heat treatment at 0.23 V vs Ag/AgCl under 1 Sun illumination.

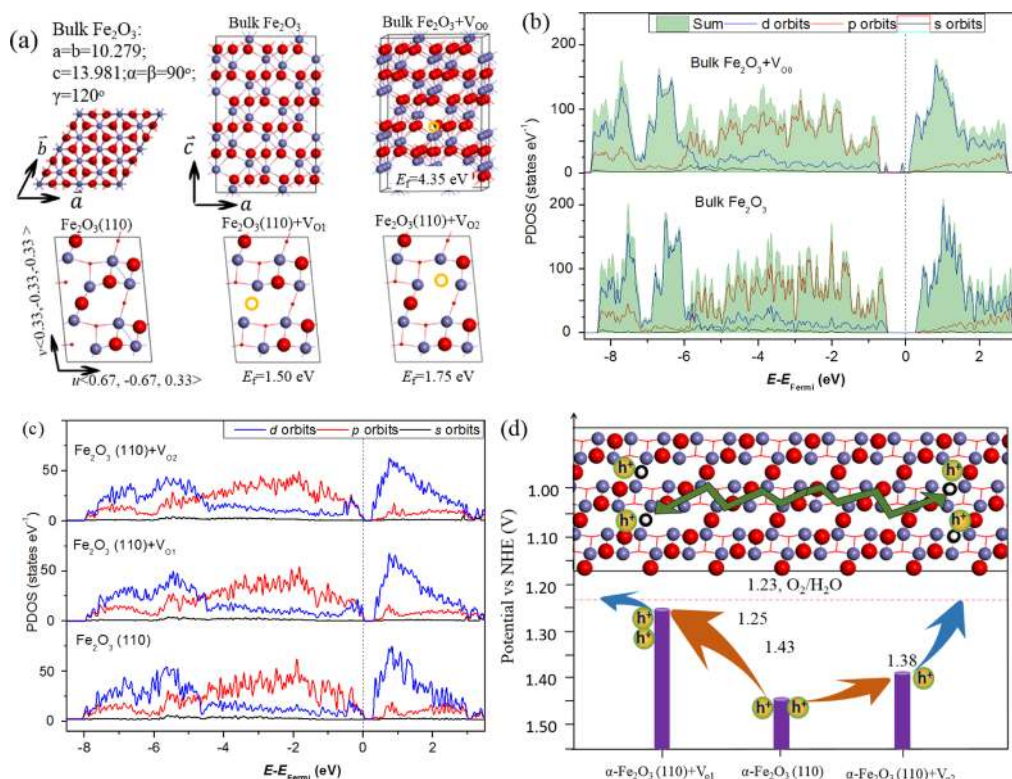


**Figure 4.** (a) Optimized geometric structures of bulk  $\alpha\text{-Fe}_2\text{O}_3$ ,  $\alpha\text{-Fe}_2\text{O}_3$  (110) facet, and  $\alpha\text{-Fe}_2\text{O}_3$  (110) facet with  $\text{V}_\text{O}$ . The formation energy of  $\text{V}_\text{O}$  is also manifested. (b) PDOS of bulk  $\alpha\text{-Fe}_2\text{O}_3$  and bulk  $\alpha\text{-Fe}_2\text{O}_3$  with  $\text{V}_\text{O}$  and (c) PDOS of  $\alpha\text{-Fe}_2\text{O}_3$  (110) facet and  $\alpha\text{-Fe}_2\text{O}_3$  (110) facet with  $\text{V}_\text{O}$ . (d) Calculated edges relative to the NHE potential at pH = 0, where the charge-transport process on the surface is also added; Fe, O, and  $\text{V}_\text{O}$  atoms are shown as blue, red, and hollow yellow spheres. More details about the potential can be found in the Supporting Information (Figure S2).

respectively.  $A$ ,  $N_\text{d}$ ,  $V$ , and  $C$  are the area of the  $\alpha\text{-Fe}_2\text{O}_3$  film, the charge carrier density, the bias applied on the electrode, and the surface capacitance, respectively. Although this equation is used for planar electrodes and may not provide a precise quantitative analysis for the nanorod structure, comparison between the treated and untreated samples would still provide an indication of the change of carrier density because of the presence of  $\text{V}_\text{O}$ . Our analysis indicates the carrier densities after air and N<sub>2</sub> heat treatment to be  $3.2 \times 10^{19}$  and  $4.6 \times 10^{19} \text{ cm}^{-3}$ , respectively. Therefore, N<sub>2</sub> heat treatment enhances the carrier density because of the generation of  $\text{V}_\text{O}$ .



The  $\text{V}_\text{O}$  concentration,  $n_\text{v}$ , of  $\alpha\text{-Fe}_2\text{O}_3$  is determined by the oxygen partial pressure,  $p_{\text{O}_2}$ , as  $n_\text{v} \propto p_{\text{O}_2}^{-1/6}$ .<sup>40</sup> Thus, nitrogen treatment introduces  $\text{V}_\text{O}$  because of the low  $p_{\text{O}_2}$ . It was reported that  $\text{V}_\text{O}$  can be generated in  $\alpha\text{-Fe}_2\text{O}_3$  when annealed in argon or nitrogen gas.<sup>36</sup> According to eq 2, the generation of  $\text{V}_\text{O}$  will induce more free electrons. Thus,  $\text{V}_\text{O}$  can be considered as a shallow donor for  $\alpha\text{-Fe}_2\text{O}_3$ .<sup>41–43</sup>

Electrochemical impedance spectroscopy (EIS) was used to characterize hole transfer across the electrode/electrolyte interface. Figure 3b shows the EIS data of  $\alpha\text{-Fe}_2\text{O}_3$  after air and N<sub>2</sub> heat treatment. An equivalent circuit (Figure 3b) was used to fit the EIS data, where  $R_\text{s}$  is the solution resistance;  $R_\text{trap}$  denotes the resistance of the surface state trapping holes;  $C_\text{ss}$  represents the capacitance from the surface states; and  $R_\text{ss}$  denotes the charge-transfer resistance. The result indicates that



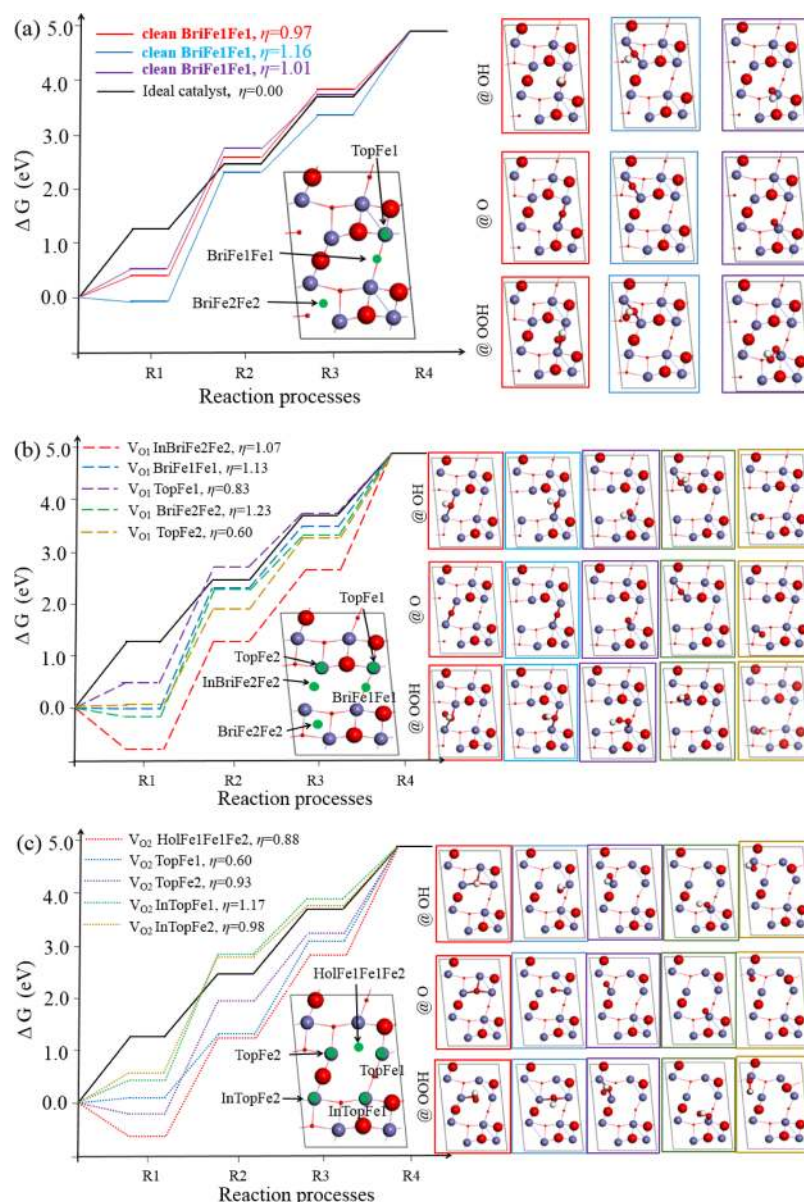


**Figure 5.** Free energy profiles and adsorption structures of OER on different surfaces on different active sites, where green spheres indicate the active sites, and Fe (blue), O (red), and H (white) atoms are shown in colored spheres: (a) clean  $\alpha\text{-Fe}_2\text{O}_3$  (110), (b)  $\alpha\text{-Fe}_2\text{O}_3$  (110) with  $V_{O1}$ , and (c)  $\alpha\text{-Fe}_2\text{O}_3$  (110) with  $V_{O2}$ . The unit of overpotential is V. More details are obtained from Tables S2–S4 and Figure S3.

$R_{\text{trap}}$  after the air treatment is about  $6.7 \times 10^3 \Omega$ , whereas that after the  $\text{N}_2$  treatment is  $3.4 \Omega$  (details in Table S1). Therefore, we can conclude that the number of hole-trapping surface states is greatly decreased after the  $\text{N}_2$  heat treatment. On the basis of the above analysis,  $V_O$  not only affects the conductivity but also has an effect on the surface states. Thus, further analysis is needed to understand how  $V_O$  affects the charge separation and charge-transfer processes.

**2.3. Geometric and Electronic Characteristics of  $\alpha\text{-Fe}_2\text{O}_3$ .** The geometric and electronic properties of optimized  $\alpha\text{-Fe}_2\text{O}_3$  and  $\alpha\text{-Fe}_2\text{O}_3$  (110) facet, with or without  $V_O$ , are displayed in Figure 4.

As indicated in Figure 4a, the concentration of  $V_O$  is 1.4% for the  $2 \times 2 \times 1$  supercells of  $\alpha\text{-Fe}_2\text{O}_3$ , and the surface coverage of  $V_O$  is 17% for the  $2 \times 1$  supercells of the  $\alpha\text{-Fe}_2\text{O}_3$  (110) surface. There are one type of  $V_O$  on the bulk and two types of  $V_O$  on the (110) surface because all O on the bulk  $\alpha\text{-Fe}_2\text{O}_3$  are connected with four Fe neighbors and form a

tetrahedron (denoted as  $V_{O0}$ ), whereas some of the surface O have coordination number 2 (denoted as  $V_{O1}$ ) and some have coordination number 3 (denoted as  $V_{O2}$ ). The formation energies of  $V_{O1}$  and  $V_{O2}$  are much smaller than that of  $V_{O0}$ , which means that  $V_O$  can be easily formed on the  $\alpha\text{-Fe}_2\text{O}_3$  (110) surface when compared with the bulk. Furthermore, it was found that the formation energy of  $V_O$  on the  $\alpha\text{-Fe}_2\text{O}_3$  (110) facet is smaller than that on the  $\text{TiO}_2$  (110) facets (3.55 eV).<sup>44</sup> As well-known,  $\text{TiO}_2$  can easily generate  $V_O$ , which means  $V_O$  can also be easily formed on the  $\alpha\text{-Fe}_2\text{O}_3$  (110) facet. The band structure of bulk  $\alpha\text{-Fe}_2\text{O}_3$  and bulk  $\alpha\text{-Fe}_2\text{O}_3 + V_O$  are presented as partial density of states (PDOS) plots, as shown in Figure 4b. It shows that the valence band maximum is mainly composed of Fe 3d and O 2p resonance peaks, whereas the conduction band minimum is largely constituted by Fe 3d orbitals. This means that the electrons are generated from the bond of Fe 3d and O 2p orbitals to the bond of Fe 3d orbitals, and this behavior will generate photogenerated holes

on the valence band maximum. Furthermore,  $V_O$  in bulk  $\alpha\text{-Fe}_2\text{O}_3$  will greatly change the band structure. As shown in Figure 4b, the  $V_O$  defects in bulk  $\alpha\text{-Fe}_2\text{O}_3$  will introduce two deep-level states in the band gap. Empirically, a midgap ground state can be considered as a recombination center (the Shockley–Read–Hall effect).<sup>45</sup> Therefore, the  $V_O$  defects in the bulk  $\alpha\text{-Fe}_2\text{O}_3$  will shorten the lifetime of the generated holes. Fortunately, the formation energy for  $V_O$  generation in the bulk  $\alpha\text{-Fe}_2\text{O}_3$  is very high; therefore, in practical terms, the density of such defects will be low. On the surfaces, the Fermi levels of the  $\alpha\text{-Fe}_2\text{O}_3$  (110) facets, with and without  $V_O$ , are located at the valence band maximum (Figure 4c). This means that the electron carrier density is not greatly improved by the presence of  $V_O$  on the surface. Furthermore, the normal hydrogen electrode (NHE) potential indicates that the surface potential for the  $\alpha\text{-Fe}_2\text{O}_3$  (110) +  $V_O$  facet is greatly reduced, as indicated in Figure 4d. It reveals that holes can be easily transferred from the defect-free surface to the defect surface. Therefore, the enhanced charge separation mainly comes from the potential change on the surface. A similar finding was reported in the  $\text{BiVO}_4$  (010) facet.<sup>46</sup>

**2.4. Adsorption Properties of  $\alpha\text{-Fe}_2\text{O}_3$ .** The energy change,  $\Delta G$ , for the adsorption of OH (denoted as @OH) is lower than the ideal catalysis, indicating OH is easily adsorbed on the  $\alpha\text{-Fe}_2\text{O}_3$  (110) surface. The high adsorption energies of @OH make it difficult to lose a H adatom and generate O adatom. Therefore, the rate-determining step is the loss of H adatom for @OH, except for the  $V_{O2}$  TopFe1 site. For the TopFe1 site, the rate-determining step is the loss of H adatom on another  $\text{H}_2\text{O}$  to form @OOH. No matter which step is the determining step, the theoretical overpotential can be adopted to assess the OER activity. Figure 5a shows the bridge site Fe1Fe1, bridge site Fe2Fe2, and top site Fe1, which are the active sites for the clean  $\alpha\text{-Fe}_2\text{O}_3$  surface, with an overpotential of 0.97, 1.16, and 1.01 V, respectively. After introducing  $V_O$  on the surface, the overpotential increases on some active sites such as the bridge Fe1Fe1 and bridge Fe2Fe2, whereas it decreases on the top Fe1 site (Figure 5b,c). The overpotentials for the defect-free,  $V_{O1}$  site, and  $V_{O2}$  sites are 1.05, 0.97, and 0.91 V, respectively. Considering the errors in this type of calculation, it can be concluded that on average, the overpotentials for the defect-free surface and the  $V_O$  surface are very close to each other. This is consistent with the experimental evidence in Figure 2 that the onset potentials of the samples treated in air and nitrogen atmosphere are close to each other.

The presence of  $V_O$  was found to be able to increase the stable adsorption sites. The bridge Fe2Fe2 and top Fe2 sites on the  $V_{O1}$  surface have become active in the presence of  $V_O$ . Thus, we understand that the main function of  $V_O$  is to generate more active sites on the surface (experimentally, this has increased the photocurrent density by about 137%). Comparing the Gibbs free energy, it clearly indicates that the OER on the  $\alpha\text{-Fe}_2\text{O}_3$  (110) surface is mainly determined by R1–R2 because the slope of this process is higher than that of an ideal catalysis process. On the basis of the above analyses, the mechanism of improved photocurrent by  $\text{N}_2$  treatment is mainly attributed to the generated  $V_O$  on the surface. The  $V_O$  on the surface can greatly improve the surface potential and then improve the hole transfer on the surface. Furthermore, the presence of  $V_O$  also increased the density of the active sites. These two reasons can reasonably explain the improved

performance of photocurrent by  $\text{N}_2$  treatment on the  $\alpha\text{-Fe}_2\text{O}_3$  (110) surface.

### 3. CONCLUSIONS

In summary, we carried out comprehensive experimental and theoretical studies on the roles of  $V_O$  on  $\alpha\text{-Fe}_2\text{O}_3$  (110) photoanode. The experimental results indicate that  $\text{N}_2$  treatment has enhanced the photocurrent significantly. The enhancement mainly comes from a better charge separation and an enhanced surface charge transfer. Combining the experimental results with the density functional theory (DFT) calculations, we found that the improved charge separation is contributed by the increased electron density and the surface potential change. The enhanced surface charge transfer is mainly because of the increased density of active sites. This research provides improved insights into the roles of  $V_O$  on surface catalysis.

### 4. EXPERIMENTAL DETAILS

**4.1. Preparation of  $\text{Fe}_2\text{O}_3$  Thin Films.** Pristine  $\text{Fe}_2\text{O}_3$  film electrodes were prepared by a hydrothermal method. A 0.49 g  $\text{FeCl}_3$  and 1.70 g  $\text{NaNO}_3$  were added into a 20 mL aqueous solution and then transferred onto a Teflon vial with a capacity of 40 mL. A proper amount of HCl with 3.7% concentration was added to adjust the pH value. A piece of glass substrate with a fluorine-doped  $\text{SnO}_2$  coating was covered by a thermal tape with half of the conductive side exposed and placed inside the vial. After heating at 95 °C for 6 h, the vessel was cooled to room temperature, and the obtained thin-film electrode was washed by using deionized water and then heated under ambient environment at 700 °C for 20 min to obtain a layer of  $\text{Fe}_2\text{O}_3$  nanorods. The nitrogen treatment was performed at 500 °C for 2 h with a pure nitrogen gas flow rate of 50 sccm in a vacuumed tube furnace.

**4.2. Characterization.** The hematite nanorod film electrodes' morphologies and thickness were recorded on a field emission scanning electron microscope (JEOL JSM-7600F). The powder XRD data were characterized by a Shimadzu 6000 X-ray diffractometer with  $\text{Cu K}\alpha$  radiation ( $\lambda = 0.154$  nm). The SAED patterns were recorded using a transmission electron microscope (JEOL JEM-2010F). The light absorption was measured with a UV–vis–near-infrared spectrophotometer (LAMBDA 950, PerkinElmer). A conventional three-electrode system (PCI4/300 potentiostat, Gamry Electronic Instruments, Inc.) was used for the photocurrent measurement, where hematite film is the working electrode, Pt mesh is the counter electrode, and Ag/AgCl is the reference electrode. The light source was an AM 1.5G solar simulator (HAL-320, Asahi Spectra Co., Ltd.) with an intensity of  $100 \text{ mW}\cdot\text{cm}^{-2}$  calibrated by a solar reference cell. The illumination area was  $0.28 \text{ cm}^2$  in 1 M NaOH aqueous (pH = 13.6) solution with a scan rate of  $30 \text{ mV}\cdot\text{s}^{-1}$ . An Autolab potentiostat–galvanostat (Autolab PGSTAT302 N) was employed to measure the electrochemical impedance spectra and Mott–Schottky plots.

The photocurrent of water oxidation ( $J_{\text{H}_2\text{O}}$ ) is indicated in eq 3<sup>47</sup>

$$J_{\text{H}_2\text{O}} = J_0 \times \eta_{\text{abs}} \times \eta_{\text{sep}} \times \eta_{\text{tran}} = J_{\text{abs}} \times \eta_{\text{sep}} \times \eta_{\text{tran}} \quad (3)$$

where  $J_0$  is the theoretical solar photocurrent ( $12.5 \text{ mA}\cdot\text{cm}^{-2}$  for  $\text{Fe}_2\text{O}_3$ ).<sup>48</sup>  $\eta_{\text{abs}}$ ,  $\eta_{\text{sep}}$ , and  $\eta_{\text{tran}}$  are the efficiency of light absorption, charge separation, and interfacial charge transfer, respectively.

To quantitatively analyze the contributions,  $\text{Na}_2\text{SO}_3$  was utilized to suppress the charge recombination on the surface.  $\eta_{\text{trans}}$  can be considered as 1 when hole scavenger  $\text{Na}_2\text{SO}_3$  is added. Thus, the  $\text{Na}_2\text{SO}_3$  oxidation photocurrent is determined by eq 4

$$J_{\text{Na}_2\text{SO}_3} = J_0 \times \eta_{\text{abs}} \times \eta_{\text{sep}} = J_{\text{abs}} \times \eta_{\text{sep}} \quad (4)$$

where  $J_{\text{Na}_2\text{SO}_3}$  is the measured photocurrent in  $\text{Na}_2\text{SO}_3$  solution. On the basis of the light absorption efficiencies,  $J_{\text{abs}}$  is about  $11.3 \text{ mA}\cdot\text{cm}^{-2}$  for our  $\alpha\text{-Fe}_2\text{O}_3$ , as shown in Figure S4. From eqs 3 and 4,  $\eta_{\text{sep}} = J_{\text{Na}_2\text{SO}_3}/J_{\text{abs}}$  and  $\eta_{\text{tran}} = J_{\text{H}_2\text{O}}/J_{\text{Na}_2\text{SO}_3}$ .

## 5. COMPUTATIONAL DETAILS

The DFT simulations of generalized gradient approximation and the Perdew–Burke–Ernzerhof functional were used in the CASTEP module. The Broyden–Fletcher–Goldfarb–Shanno method is adopted as the quasi-Newton optimization technique. The partially filled and strongly correlated localized d electrons of Fe were treated using Hubbard  $U$ -corrections with  $U(V) = 2.5 \text{ eV}$ .<sup>49,50</sup> The expression for dispersion correction is calculated by the method of Tkatchenko and Scheffler. Ultrasoft pseudopotentials in reciprocal space were used with an energy cutoff of 340 eV and a self-consistent field tolerance of  $1.0 \times 10^{-6} \text{ eV}\cdot\text{atom}^{-1}$ , where the valence electron configurations were set as  $\text{Fe-}3\text{d}^6 4\text{s}^2$ ,  $\text{O-}2\text{s}^2 2\text{p}^4$ . The structure optimization was finished when the energy, force, and displacement were smaller than  $1.0 \times 10^{-5} \text{ eV}\cdot\text{atom}^{-1}$ ,  $0.03 \text{ eV}\cdot\text{\AA}^{-1}$ ,  $0.05 \text{ GPa}$ , and  $0.001 \text{ \AA}$ .  $\alpha\text{-Fe}_2\text{O}_3$  (space group 167) and the corresponding  $1 \times 2 (110)$  facet with five layers and a vacuum region of  $15 \text{ \AA}$  were constructed. These numbers of layers were found to be sufficient for the convergence of the final result on the basis of surface energy calculations (Figure S5). The  $3 \times 3 \times 2$  and  $2 \times 1 \times 1$   $k$ -points sampling was adopted for the bulk and surface calculations, and the optimized structure is consistent with previous results (Table S5).

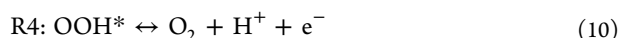
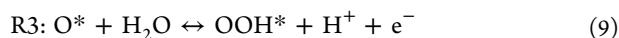
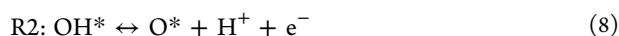
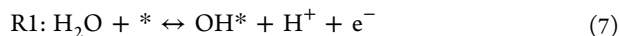
The formation energy of  $\text{V}_\text{O}$  ( $E_{\text{vf}}$ ) and the adsorption energy ( $E_{\text{ads}}$ ) can be calculated through eqs 5 and 6

$$E_{\text{vf}} = E_{\text{ds}} + E_{\text{O}_2} - E_{\text{ps}} \quad (5)$$

$$E_{\text{ads}} = E_{\text{molecule+surface}} - E_{\text{molecule}} - E_{\text{surface}} \quad (6)$$

where  $E_{\text{ds}}$ ,  $E_{\text{ps}}$ ,  $E_{\text{O}_2}$ ,  $E_{\text{molecule+surface}}$ ,  $E_{\text{molecule}}$ , and  $E_{\text{surface}}$  are the optimized energies of the defective surface, perfect surface,  $\text{O}_2$  molecule in gas state, surface with the adsorbent, adsorption molecules, and the surface, respectively.<sup>51</sup>

As known, the water-splitting process can happen with the R1–R4 reaction paths, where \* represents a surface site.<sup>52,53</sup>



The standard Gibbs free energy of R1–R4 is obtained by 11

$$\Delta G_{\text{R1}}^\theta = \Delta G_{\text{OH}} \quad (11)$$

$$\Delta G_{\text{R2}}^\theta = \Delta G_{\text{O}} - \Delta G_{\text{OH}} \quad (12)$$

$$\Delta G_{\text{R3}}^\theta = \Delta G_{\text{OOH}} - \Delta G_{\text{O}} \quad (13)$$

$$\Delta G_{\text{R4}}^\theta = \Delta G_{\text{O}_2(\text{g})}^\theta - \Delta G_{\text{OOH}} \quad (14)$$

The theoretical overpotential is expressed as

$$\eta = \max(\Delta G_{\text{Ri}}^\theta)/e - 1.23 \quad (15)$$

where  $\Delta G_{\text{O}}$ ,  $\Delta G_{\text{OH}}$ ,  $\Delta G_{\text{OOH}}$ , and  $\Delta G_{\text{O}_2}$  are the adsorption energies of the corresponding adsorbates, including contributions from the vibrational energy and entropy at 300 K. The details of the calculation can be found in our previous paper.<sup>54</sup>

## ■ ASSOCIATED CONTENT

### Supporting Information

The Supporting Information is available free of charge on the ACS Publications website at DOI: 10.1021/acsomega.8b01195.

Light absorption efficiency, simulation verification, work function, and data for adsorption (PDF)

## ■ AUTHOR INFORMATION

### Corresponding Authors

\*E-mail: xinzha@ntu.edu.sg (X.Z.).

\*E-mail: ASZChen@ntu.edu.sg (Z.C.).

### ORCID

Jun Hu: 0000-0002-3075-9291

Xin Zhao: 0000-0002-7493-1014

Zhong Chen: 0000-0001-7518-1414

### Author Contributions

<sup>||</sup>J.H. and X.Z. contributed equally to this work.

### Notes

The authors declare no competing financial interest.

## ■ ACKNOWLEDGMENTS

Financial support from the Ministry of Education of Singapore (RG15/16), the National Natural Science Foundation of China (no. 21676216), China Postdoctoral Science Foundation (no. 2014M550507; 2015T81046), and the Innovative Projects of Northwest University (YZZ17140) is gratefully acknowledged. Technical support from Dr. Weiling Liu from FACTS, NTU is very much appreciated.

## ■ REFERENCES

- (1) Lu, X.-F.; Chen, X.-Y.; Zhou, W.; Tong, Y.-X.; Li, G.-R.  $\alpha\text{-Fe}_2\text{O}_3$ @PANI Core–Shell Nanowire Arrays as Negative Electrodes for Asymmetric Supercapacitors. *ACS Appl. Mater. Interfaces* **2015**, *7*, 14843–14850.
- (2) Hardee, K. L.; Bard, A. Semiconductor Electrodes V. The Application of Chemically Vapor Deposited Iron Oxide Films to Photosensitized Electrolysis. *J. Electrochem. Soc.* **1976**, *123* (7), 1024–1026.
- (3) Luo, Z.; Li, C.; Liu, S.; Wang, T.; Gong, J. Gradient Doping of Phosphorus in  $\text{Fe}_2\text{O}_3$  Nanoarray Photoanodes for Enhanced Charge Separation. *Chem. Sci.* **2017**, *8*, 91–100.
- (4) Zhang, R.; Yang, L.; Huang, X.; Chen, T.; Qu, F.; Liu, Z.; Du, G.; Asiri, A. M.; Sun, X. Se Doping: an Effective Strategy Toward  $\text{Fe}_2\text{O}_3$  Nanorod Arrays for Greatly Enhanced Solar Water Oxidation. *J. Mater. Chem. A* **2017**, *5*, 12086–12090.
- (5) Lee, C.-Y.; Wang, L.; Kado, Y.; Kirchgeorg, R.; Schmuki, P. Si-doped  $\text{Fe}_2\text{O}_3$  Nanotubular/nanoporous Layers for Enhanced Photoelectrochemical Water Splitting. *Electrochem. Commun.* **2013**, *34*, 308–311.



- (6) Hensley, A. J. R.; Hong, Y.; Zhang, R.; Zhang, H.; Sun, J.; Wang, Y.; McEwen, J.-S. Enhanced  $\text{Fe}_2\text{O}_3$  Reducibility via Surface Modification with Pd: Characterizing the Synergy within Pd/Fe Catalysts for Hydrodeoxygenation Reactions. *ACS Catal.* **2014**, *4*, 3381–3392.
- (7) Cho, I. S.; Han, H. S.; Logar, M.; Park, J.; Zheng, X. Solar Water Splitting: Enhancing Low-Bias Performance of Hematite Photoanodes for Solar Water Splitting by Simultaneous Reduction of Bulk, Interface, and Surface Recombination Pathways. *Adv. Energy Mater.* **2016**, *6*, 1501840.
- (8) Annamalai, A.; Shinde, P. S.; Subramanian, A.; Kim, J. Y.; Kim, J. H.; Choi, S. H.; Lee, J. S.; Jang, J. S. Bifunctional  $\text{TiO}_2$  Underlayer for  $\alpha\text{-Fe}_2\text{O}_3$  Nanorod Based Photoelectrochemical Cells: Enhanced Interface and  $\text{Ti}^{4+}$  Doping. *J. Mater. Chem. A* **2015**, *3*, 5007–5013.
- (9) Deng, J.; Zhong, J.; Pu, A.; Zhang, D.; Li, M.; Sun, X.; Lee, S.-T. Ti-Doped Hematite Nanostructures for Solar Water Splitting with High Efficiency. *J. Appl. Phys.* **2012**, *112*, 084312.
- (10) Cao, D.; Luo, W.; Feng, J.; Zhao, X.; Li, Z.; Zou, Z. Cathodic Shift of Onset Potential for Water Oxidation on a  $\text{Ti}^{4+}$  Doped  $\text{Fe}_2\text{O}_3$  Photoanode by Suppressing the Back Reaction. *Energy Environ. Sci.* **2014**, *7*, 752–759.
- (11) Tang, X.; Jia, R.; Zhai, T.; Xia, H. Hierarchical  $\text{Fe}_3\text{O}_4/\text{Fe}_2\text{O}_3$  Core–Shell Nanorod Arrays as High-Performance Anodes for Asymmetric Supercapacitors. *ACS Appl. Mater. Interfaces* **2015**, *7*, 27518–27525.
- (12) Wang, L. L.; Fei, T.; Lou, Z.; Zhang, T. Three-Dimensional Hierarchical Flowerlike  $\alpha\text{-Fe}_2\text{O}_3$  Nanostructures: Synthesis and Ethanol-Sensing Properties. *ACS Appl. Mater. Interfaces* **2011**, *3*, 4689–4694.
- (13) Tilley, S. D.; Cornuz, M.; Sivula, K.; Grätzel, M. Light-Induced Water Splitting with Hematite: Improved Nanostructure and Iridium Oxide Catalysis. *Angew. Chem.* **2010**, *122*, 6549–6552.
- (14) Sharp, I. D.; Cooper, J. K.; Toma, F. M.; Buonsanti, R. Bismuth Vanadate as a Platform for Accelerating Discovery and Development of Complex Transition-Metal Oxide Photoanodes. *ACS Energy Lett.* **2017**, *2*, 139–150.
- (15) Campbell, T. C.; Peden, C. H. F. Oxygen Vacancies and Catalysis on Ceria Surfaces. *Science* **2005**, *309*, 713–714.
- (16) Tompsett, D. A.; Parker, S. C.; Islam, M. S. Rutile ( $\beta$ -)  $\text{MnO}_2$  Surfaces and Vacancy Formation for High Electrochemical and Catalytic Performance. *J. Am. Chem. Soc.* **2014**, *136*, 1418–1426.
- (17) Cheng, F.; Zhang, T.; Zhang, Y.; Du, J.; Han, X.; Chen, J. Enhancing Electrochemical Oxygen Reduction on  $\text{MnO}_2$  with Vacancies. *Angew. Chem., Int. Ed.* **2013**, *52*, 2474–2477.
- (18) Wang, G.; Ling, Y.; Wang, H.; Yang, X.; Wang, C.; Zhang, J. Z.; Li, Y. Hydrogen-treated  $\text{WO}_3$  Nanoflakes Show Enhanced Photostability. *Energy Environ. Sci.* **2012**, *5*, 6180–6187.
- (19) Gan, J.; Lu, X.; Rajeeva, B. B.; Menz, R.; Tong, Y.; Zheng, Y. Efficient Photoelectrochemical Water Oxidation over Hydrogen-Reduced Nanoporous  $\text{BiVO}_4$  with Ni–Bi Electrocatalyst. *ChemElectroChem* **2015**, *2*, 1385–1395.
- (20) Singh, A. P.; Kodan, N.; Dey, A.; Krishnamurthy, S.; Mehta, B. R. Improvement in the Structural, Optical, Electronic and Photoelectrochemical Properties of Hydrogen Treated Bismuth Vanadate Thin Films. *Int. J. Hydrogen Energy* **2015**, *40*, 4311–4319.
- (21) Bjørheim, T. S.; Kotomin, E. Ab Initio Thermodynamics of Oxygen Vacancies and Zinc Interstitials in  $\text{ZnO}$ . *J. Phys. Chem. Lett.* **2014**, *5*, 4238–4242.
- (22) Deml, A. M.; Holder, A. M.; O’Hayre, R. P.; Musgrave, C. B.; Stevanović, V. Intrinsic Material Properties Dictating Oxygen Vacancy Formation Energetics in Metal Oxides. *J. Phys. Chem. Lett.* **2015**, *6*, 1948–1953.
- (23) Kong, M.; Li, Y.; Chen, X.; Tian, T.; Fang, P.; Zheng, F.; Zhao, X. Tuning the Relative Concentration Ratio of Bulk Defects to Surface Defects in  $\text{TiO}_2$  Nanocrystals Leads to High Photocatalytic Efficiency. *J. Am. Chem. Soc.* **2011**, *133*, 16414–16417.
- (24) Zhao, H.; Wang, J.; Zhang, L.; Rong, Y.; Chen, J.; Ibrahim, K.; Xing, X. Effects of Oxygen Vacancy on the Electronic Structure and Multiferroics in Sol–gel Derived  $\text{Pb}_{0.8}\text{Co}_{0.2}\text{TiO}_3$  Thin Films. *Dalton Trans.* **2013**, *42*, 10358–10364.
- (25) Kim, T. W.; Ping, Y.; Galli, G. A.; Choi, K.-S. Simultaneous Enhancements in Photon Absorption and Charge Transport of Bismuth Vanadate Photoanodes for Solar Water Splitting. *Nat. Commun.* **2015**, *6*, 8769.
- (26) Ling, Y.; Wang, G.; Reddy, J.; Wang, C.; Zhang, J. Z.; Li, Y. The Influence of Oxygen Content on the Thermal Activation of Hematite Nanowires. *Angew. Chem.* **2012**, *124*, 4150–4155.
- (27) Dieckmann, R. Point Defects and Transport in Hematite ( $\text{Fe}_2\text{O}_3\text{-}\epsilon$ ). *Philos. Mag. A* **1993**, *68*, 725–745.
- (28) Chen, Z.; Cvelbar, U.; Mozetič, M.; He, J.; Sunkara, M. K. Long-Range Ordering of Oxygen-Vacancy Planes in  $\alpha\text{-Fe}_2\text{O}_3$  Nanowires and Nanobelts. *Chem. Mater.* **2008**, *20*, 3224–3228.
- (29) Warschkow, O.; Ellis, D. E.; Hwang, J.; Mansourian-Hadavi, N.; Mason, T. O. Defects and Charge Transport near the Hematite (0001) Surface: An Atomistic Study of Oxygen Vacancies. *J. Am. Ceram. Soc.* **2002**, *85*, 213–220.
- (30) Hoh, S. W.; Thomas, L.; Jones, G.; Willock, D. J. A Density Functional Study of Oxygen Vacancy Formation on  $\alpha\text{-Fe}_2\text{O}_3$  (0001) Surface and the Effect of Supported Au Nanoparticles. *Res. Chem. Intermed.* **2015**, *41*, 9587–9601.
- (31) Song, Z.; Wang, B.; Yu, J.; Ma, C.; Zhou, C.; Chen, T.; Yan, Q.; Wang, K.; Sun, L. Density Functional Study on the Heterogeneous Oxidation of NO Over  $\text{Fe}_2\text{O}_3$  Catalyst by  $\text{H}_2\text{O}_2$ : Effect of Oxygen Vacancy. *Appl. Surf. Sci.* **2017**, *413*, 292–301.
- (32) Tolod, K.; Hernández, S.; Russo, N. Recent Advances in the  $\text{BiVO}_4$  Photocatalyst for Sun-Driven Water Oxidation: Top-Performing Photoanodes and Scale-Up Challenges. *Catalysts* **2017**, *7*, 13.
- (33) Yang, J.; Wang, D.; Zhou, X.; Li, C. A Theoretical Study on the Mechanism of Photocatalytic Oxygen Evolution on  $\text{BiVO}_4$  in Aqueous Solution. *Chem.—Eur. J.* **2013**, *19*, 1320–1326.
- (34) Zhao, Z.-Y. Single Water Molecule Adsorption and Decomposition on the Low-Index Stoichiometric Rutile  $\text{TiO}_2$  Surfaces. *J. Phys. Chem. C* **2014**, *118*, 4287–4295.
- (35) Zhang, X.; Klaver, P.; van Santen, R.; van de Sanden, M. C. M.; Bieberle-Hüttner, A. Oxygen Evolution at Hematite Surfaces: The Impact of Structure and Oxygen Vacancies on Lowering the Overpotential. *J. Phys. Chem. C* **2016**, *120*, 18201–18208.
- (36) Wang, Y.; Feng, C.; Zhang, M.; Yang, J.; Zhang, Z. Enhanced Visible Light Photocatalytic Activity of N-doped  $\text{TiO}_2$  in Relation to Single-electron-trapped Oxygen Vacancy and Doped-nitrogen. *Appl. Catal., B* **2010**, *100*, 84–90.
- (37) Wang, J.; Wang, Z.; Huang, B.; Ma, Y.; Liu, Y.; Qin, X.; Zhang, X.; Dai, Y. Oxygen Vacancy Induced Band-Gap Narrowing and Enhanced Visible Light Photocatalytic Activity of  $\text{ZnO}$ . *ACS Appl. Mater. Interfaces* **2012**, *4*, 4024–4030.
- (38) Zhao, X.; Feng, J.; Chen, S.; Huang, Y.; Sum, T. C.; Chen, Z. New Insight into the Roles of Oxygen Vacancies in Hematite for Solar Water Splitting. *Phys. Chem. Chem. Phys.* **2017**, *19*, 1074–1082.
- (39) Cesar, I.; Sivula, K.; Kay, A.; Zboril, R.; Grätzel, M. Influence of Feature Size, Film Thickness, and Silicon Doping on the Performance of Nanostructured Hematite Photoanodes for Solar Water Splitting. *J. Phys. Chem. C* **2008**, *113*, 772–782.
- (40) Steier, L.; Herraiz-Cardona, I.; Gimenez, S.; Fabregat-Santiago, F.; Bisquert, J.; Tilley, S. D.; Grätzel, M. Understanding the Role of Underlayers and Overlayers in Thin Film Hematite Photoanodes. *Adv. Funct. Mater.* **2014**, *24*, 7681–7688.
- (41) Le Formal, F.; Tétreault, N.; Cornuz, M.; Moehl, T.; Grätzel, M.; Sivula, K. Passivating Surface States on Water Splitting Hematite Photoanodes with Alumina Overlayers. *Chem. Sci.* **2011**, *2*, 737–743.
- (42) Yang, T.-Y.; Kang, H.-Y.; Sim, U.; Lee, Y.-J.; Lee, J.-H.; Koo, B.; Nam, K. T.; Joo, Y.-C. A New Hematite Photoanode Doping Strategy for Solar Water Splitting: Oxygen Vacancy Generation. *Phys. Chem. Chem. Phys.* **2013**, *15*, 2117–2124.
- (43) Pu, A.; Deng, J.; Li, M.; Gao, J.; Zhang, H.; Hao, Y.; Zhong, J.; Sun, X. Coupling Ti-Doping and Oxygen Vacancies in Hematite Nanostructures for Solar Water Oxidation with High Efficiency. *J. Mater. Chem. A* **2014**, *2*, 2491–2497.



- (44) Wu, X.; Selloni, A.; Nayak, S. K. First Principles Study of CO Oxidation on  $\text{TiO}_2$  (110): The Role of Surface Oxygen Vacancies. *J. Chem. Phys.* **2004**, *120*, 4512–4516.
- (45) Hall, R. N. Electron-hole Recombination in Germanium. *Phys. Rev.* **1952**, *87*, 387.
- (46) Hu, J.; Chen, W.; Zhao, X.; Su, H.; Chen, Z. Anisotropic Electronic Characteristics, Adsorption, and Stability of Low-index  $\text{BiVO}_4$  Surfaces for Photoelectrochemical Applications. *ACS Appl. Mater. Interfaces* **2018**, *10*, 5475–5484.
- (47) Dotan, H.; Sivula, K.; Grätzel, M.; Rothschild, A.; Warren, S. C. Probing the Photoelectrochemical Properties of Hematite ( $\alpha\text{-Fe}_2\text{O}_3$ ) Electrodes using Hydrogen Peroxide as a Hole Scavenger. *Energy Environ. Sci.* **2011**, *4*, 958–964.
- (48) Sivula, K.; Le Formal, F.; Grätzel, M. Solar Water Splitting: Progress Using Hematite ( $\alpha\text{-Fe}_2\text{O}_3$ ) Photoelectrodes. *ChemSusChem* **2011**, *4*, 432–449.
- (49) Huang, X.; Ramadugu, S. K.; Mason, S. E. Surface-Specific DFT + U Approach Applied to  $\alpha\text{-Fe}_2\text{O}_3$ (0001). *J. Phys. Chem. C* **2016**, *120*, 4919–4930.
- (50) Emery, A. A.; Saal, J. E.; Kirklin, S.; Hegde, V. I.; Wolverton, C. High-Throughput Computational Screening of Perovskites for Thermochemical Water Splitting Applications. *Chem. Mater.* **2016**, *28*, 5621–5634.
- (51) Huang, Z.-Q.; Long, B.; Chang, C.-R. A Theoretical Study on the Catalytic Role of Water in Methanol Steam Reforming on  $\text{PdZn}(111)$ . *Catal. Sci. Technol.* **2015**, *5*, 2935–2944.
- (52) Inoue, H.; Shimada, T.; Kou, Y.; Nabetani, Y.; Masui, D.; Takagi, S.; Tachibana, H. The Water Oxidation Bottleneck in Artificial Photosynthesis: How can We Get through It? An Alternative Route Involving a Two-Electron Process. *ChemSusChem* **2011**, *4*, 173–179.
- (53) Seitz, L. C.; Dickens, C. F.; Nishio, K.; Hikita, Y.; Montoya, J.; Doyle, A.; Kirk, C.; Vojvodic, A.; Hwang, H. Y.; Nørskov, J. K.; Jaramillo, T. F. A Highly Active and Stable  $\text{IrO}_x/\text{SrIrO}_3$  Catalyst for the Oxygen Evolution Reaction. *Science* **2016**, *353*, 1011–1014.
- (54) Hu, J.; Zhao, X.; Chen, W.; Su, H.; Chen, Z. Theoretical Insight into the Mechanism of Photoelectrochemical Oxygen Evolution Reaction on  $\text{BiVO}_4$  Anode with Oxygen Vacancy. *J. Phys. Chem. C* **2017**, *121*, 18702–18709.